

# Combinatorial nuclear level-density model

H. Uhrenholt<sup>1</sup>, S. Åberg<sup>1</sup>, P. Möller<sup>2</sup>, T. Ichikawa<sup>3</sup>

<sup>1</sup>*Division of Mathematical Physics, LTH, Lund University, P.O. Box 118, S-221 00 Lund, Sweden*

<sup>2</sup>*Theoretical Division, Los Alamos National Laboratory, Los Alamos, NM 87545, USA*

<sup>3</sup>*RIKEN Nishina Center, RIKEN, Wako, Saitama 351-0198, Japan*

A microscopic nuclear level-density model is presented. The model is a completely combinatorial (micro-canonical) model based on the folded-Yukawa single-particle potential and includes explicit treatment of pairing, rotational and vibrational states. The microscopic character of all states enables extraction of level distribution functions with respect to pairing gaps, parity and angular momentum. The results of the model are compared to available experimental data: neutron separation energy level spacings, data on total level-density functions from the Oslo method, cumulative level densities from low-lying discrete states, and data on parity ratios.

## I. INTRODUCTION

Nuclear many-body level-density models are key ingredients in nuclear reaction theories, where they, for example, govern the rates and decay patterns of astrophysical processes and nuclear fission. In statistical methods, for example the Hauser-Feshbach formalism [1] for describing nuclear reactions, a knowledge of the level density is crucial [2, 3, 4]. How to calculate the nuclear level density (NLD) has been a long-standing challenge [5, 6, 7, 8, 9, 10]. Recently it has been subject to renewed interest, theoretically as well as experimentally.

The simplest type of model is the Fermi-gas model, which is based on the partition-function method. It provides simple analytical formulas for the NLD [11]. Several phenomenological extensions have been proposed in order to reproduce experimental data. By adjusting free model parameters to data these models give unprecedented accuracy in the region of the parameter fit [4, 12]. Also semi-classical methods have been used to obtain expressions for the level density [13]. However, the Fermi-gas models are unreliable outside these regions, eg. when they are extrapolated to higher excitation energies or to nucleon numbers far from stability. Ideally nuclear structure should be included in NLD models. Several combinatorial models based on nuclear mean-field theory have been proposed, see eg. Refs. [14, 15]. Beyond mean-field methods have also been used to model the NLD, eg. the Shell-Model Monte-Carlo method [16, 17] and the interacting shell model [18]. These latter models take into account effective nucleon-nucleon interactions, but at the same time suffer from limitations due to the limited size of the Hilbert space, and hence are presently unable to provide global predictions for level spacings at the neutron-separation energy.

Experimentally the NLD has been subject to renewed interest in the last decade partly due to the development of the Oslo method, which has provided new experimental data [19]. The Oslo method provides the level density over extended regions of excitation energy as opposed to the neutron-separation level-spacings data which only provide one data point at relatively high excitation energy. Also recent measurements of separate level den-

sities of  $2^+$  and  $2^-$  states [20] challenge theory to reproduce these observed parity ratios.

Few nuclear-structure models have been used to simultaneously globally describe nuclear masses, fission barriers, ground-state spins and decay rates. One such model is the microscopic-macroscopic FRLDM model which has previously been used to model these observables [3, 21, 22, 23], and here serve as the starting point for calculating the nuclear level density. In this paper a combinatorial (micro-canonical) nuclear level-density model based on the folded-Yukawa single-particle model is presented. The model is fully microscopic with pairing correlations, vibrations, and rotational excitations calculated for each many-particle-many-hole excited state. Presently, the lowest ten million or so states can be accounted for. This implies that the excitation energy region from the ground state to well above the neutron resonance region is included. No additional parameters are introduced in the model, and no refitting of parameters of the FRLDM is performed.

In Sec. II the combinatorial folded-Yukawa (CFY) level-density model is described. The model allows explicit tracking of quantum numbers, and distributions of pairing gaps, parity and angular momentum are discussed in Sec. III. Results from the CFY model are compared to experimental data in Sec. IV, and in Sec. V the CFY model is compared to other theoretical NLD models. Finally, a short summary is given in Sec. VI.

## II. THE COMBINATORIAL MODEL OF NLD (CFY)

The NLD is calculated by means of a combinatorial counting of excited many-particle-many-hole states as described in Sec. II A. In Sec. II B we present how pairing is taken into account for excited states by explicitly solving the BCS equations for all individual configurations. Rotations are taken into account combinatorially with a pairing-dependent moment of inertia (Sec. II C). The vibrational contribution to the NLD is investigated by including microscopically described phonons using the Quasi-particle Tamm-Dancoff Approximation (QTDA),

see Sec. II D. In Sec. II E it is described how we briefly account for a general residual interaction causing a smearing of the level-density distribution at higher excitation energies.

All produced nuclear levels, calculated as described below, are sorted into a binned level density, where the typical bin size is in the range  $\Delta E = 30\text{--}50$  keV. The level density is calculated by counting the number of levels in the energy bin,

$$\rho(E_b, I, \pi) = \frac{1}{\Delta E} \int_{E_b - \frac{\Delta E}{2}}^{E_b + \frac{\Delta E}{2}} \sum_i \delta(E - E_i(I, \pi)) dE, \quad (1)$$

where  $E_b$  is the energy center of bin  $b$  and  $E_i(I, \pi)$  denotes the calculated state with energy  $E_i$  (given by Eq. (15)), angular momentum  $I$  and parity  $\pi$ . The total level density at a given excitation energy  $E$  is

$$\rho_{\text{tot}}(E) = \sum_{I, \pi} \rho(E, I, \pi). \quad (2)$$

### A. Combinatorial intrinsic level density

A high-quality combinatorial level-density model requires a realistic description of the single-particle energies. We shall here utilize a well-tested mean-field model, namely the microscopic-macroscopic finite range liquid drop model (FRLDM) [21], that provides a good global description of several nuclear-structure properties such as masses, fission barriers and beta-decay properties. The good agreement between ground-state spins calculated in the FRLDM model and experiment implies that the single-particle spectrum close to the Fermi surface is well described [22].

The single-particle energies are thus obtained by solving the one-body Schrödinger equation,

$$(T + V_{FY}(\bar{\epsilon}))|\nu\rangle = e_\nu|\nu\rangle, \quad (3)$$

for protons as well as for neutrons, where  $V_{FY}$  is the Folded-Yukawa single-particle potential. The parameters of the potential, as well as the deformation parameters,  $\bar{\epsilon} = (\epsilon_2, \epsilon_3, \epsilon_4, \dots)$ , are taken from an extensive calculation of nuclear masses [21]. All parameters of the single-particle model are thus fixed from other studies. One aim of the present study is to see how well highly excited states (in terms of level-densities) are described for all nuclei heavier than  $^{16}\text{O}$ .

The many-body ground state (the many-body particle vacuum)  $|0\rangle$ , is obtained by filling the lowest  $N$  ( $Z$ ) states (including time-reversed states),

$$|0\rangle = \sum_{\nu=1}^{N(Z)} a_\nu^\dagger |-\rangle, \quad (4)$$

where  $|-\rangle$  is the one-body vacuum. Intrinsic excitations are obtained by many-particle-many-hole excitations on

the many-body particle vacuum,

$$|i\rangle = \prod_{\alpha=1}^n a_{\nu'_\alpha}^\dagger a_{\nu_\alpha} |0\rangle, \quad (5)$$

where  $\nu$  and  $\nu'$  span all single-particle states (as well as time-reversed states) in the potential. We include all  $n$ -particle- $n$ -hole states with  $n < 10$  for protons as well as for neutrons. Corresponding energies are given by

$$E_i = E_0 + \sum_{\alpha=1}^n (e_{\nu_\alpha} - e_{\nu'_\alpha}), \quad (6)$$

where  $E_0$  is the ground-state energy. (When pairing is included this expression is modified as described in Sec. II B.) Nuclei are assumed to have constant deformation for all excitation energies. For spherical and well-deformed nuclei this assumption is expected to be a good approximation for excitation energies here considered (mainly below the neutron separation energy). For transitional nuclei this approximation might, however, introduce some inaccuracies in the calculations.

In addition to the energy and the number of unpaired nucleons (seniority), we also register the total parity and  $K$ -quantum number for each excited state, where  $K$  as usual is the angular momentum projection on an intrinsic symmetry axis. The identification of a  $K$ -quantum number can be done for all nuclei by assuming an infinitesimal deformation for spherical nuclei. The  $K$ -quantum number of the individual unpaired nucleons are allowed to couple in all different ways to build up the total  $K$ -quantum number.

### B. Pairing

The many-body wave-function of the excited states is approximated by the BCS wave-function with excited quasi-particles

$$|\tau\rangle = \prod_{\nu'' \in \tau_2} (-V_{\nu''} + U_{\nu''} a_{\nu''}^\dagger a_{\bar{\nu}''}^\dagger) \times \prod_{\nu' \in \tau_1} a_{\nu'}^\dagger \prod_{\nu \in \tau_0} (U_\nu + V_\nu a_\nu^\dagger a_{\bar{\nu}}^\dagger) |0\rangle, \quad (7)$$

where  $\tau_2, \tau_1$  and  $\tau_0$  denote the spaces of double, single and zero quasi-particle excitations, respectively, used to build the many-body state  $i$  of Eq. 5.  $U_\nu$  and  $V_\nu$  are the standard BCS vacancy and occupation factors and  $|0\rangle$  is the particle vacuum, see e.g. Ref. [24]. For the excited pairs in the group  $\tau_2$  the effect (compared to zero-quasi-particle states) is simply

$$U_\nu \rightarrow -V_\nu, \quad V_\nu \rightarrow U_\nu. \quad (8)$$

The pairing gap  $\Delta$  and the Fermi energy  $\lambda$  are obtained

by solving the BCS-equations

$$\Delta = G \left[ \sum_{\nu \in \tau_0} U_\nu V_\nu - \sum_{\nu'' \in \tau_2} U_{\nu''} V_{\nu''} \right], \quad (9)$$

$$N = 2 \sum_{\nu \in \tau_0} V_\nu^2 + \sum_{\nu' \in \tau_1} 1 + 2 \sum_{\nu'' \in \tau_2} U_{\nu''}^2 \quad (10)$$

for each state.

The pairing strength in the BCS model is governed by a single, primary BCS model parameter, namely the parameter of the effective-interaction pairing gap ( $r$  in Eq.(47) in [25] or the equivalent  $c_p$  in Eq. (49) and  $c_n$  in Eq. (50) in [26]). In an adjustment of macroscopic, pairing, and other model parameters to optimize a nuclear mass model  $r = 4.8$  MeV was obtained for the standard BCS pairing model [21]. Because the BCS model we use here, in contrast to Ref. [21, 25], includes blocking and particle-number-projection it is necessary to use a pairing strength optimized for this method. In Ref. [26]  $c_p = c_n = 4.95$  MeV were obtained in an adjustment of calculated pairing gaps to odd-even mass differences. However, it has been pointed out [21, 25] that odd-even mass differences are subject to numerous non-smooth contributions, for example from deformation changes and from irregularities in the microscopic level structure, not just odd-even staggering due to pairing. It is therefore better to determine the pairing strength from a full nuclear mass calculation that includes the particular pairing model under consideration and the associated adjustment of all model parameters [21]. In the folded-Yukawa macroscopic-microscopic mass model this yields the value 4.5 MeV for the optimized strength parameter of the particle-number-projected BCS model [26]. The pairing strength  $G$ , which is used to calculate pairing gaps for all excited states in the level-density calculation, is determined from this average pairing gap for each nuclear system; for details see Ref. [26].

It follows that the excitation energy of the intrinsic many-body configuration for one nucleon type is

$$E_{\text{mb},t} = 2 \sum_{\nu \in \tau_0} e_\nu V_\nu^2 + \sum_{\nu' \in \tau_1} e_{\nu'} + 2 \sum_{\nu'' \in \tau_2} e_{\nu''} U_{\nu''}^2 - G \sum_{\nu \in \tau_0} V_\nu^4 - \frac{G}{2} \sum_{\nu' \in \tau_1} 1 - G \sum_{\nu'' \in \tau_2} U_{\nu''}^4 - \frac{\Delta^2}{G} - E_t^0, \quad (11)$$

where  $t$  denotes protons or neutrons and  $E_t^0$  is the proton or neutron part of the ground-state energy. The pairing gap and Fermi level are calculated by solving the BCS equations Eqs. (9) and (10). The total intrinsic excitation energy of a many-body state  $i$  is

$$E_{\text{mb}}^i = E_{\text{mb},p} + E_{\text{mb},n}. \quad (12)$$

The combinatorial approach to calculate the level density involves calculating all possible many-body states,  $E_{\text{mb}}^i$ , which thus means that the BCS equations are solved about  $10^7$  times for each nucleus.

### C. Rotations

A general feature of deformed nuclei is the existence of rotational bands built on the ground state as well as on excited states. The question is how to incorporate these states in the NLD. In principle, rotational states may be microscopically treated by solving the cranking Hamiltonian,  $h^\omega = h^0 - \omega_{\text{rot}} j_x$ , where  $\omega_{\text{rot}}$  is the rotational frequency and  $j_x$  is the angular momentum operator for rotations around the  $x$ -axis. Matrix elements of the  $j_x$ -operator correspond to energy excitations of the order  $\Delta E = \varepsilon_2 \hbar \omega \approx \varepsilon_2 \cdot 41 A^{-1/3}$  MeV for a nucleus with mass number  $A$  and quadrupole deformation  $\varepsilon_2$  [27]. This energy can be compared to a typical energy of lowest rotational state,  $E_{2+} = \frac{\hbar^2}{2\mathcal{J}} 2(2+1) \approx 90 A^{-5/3}$  MeV, and we see that  $\Delta E \gg E_{2+}$  for all considered nuclei. Since the collective state and the corresponding matrix element are well separated in energy, the risk of double-counting states by adding a rotational band on a microscopically calculated band-head is quite small, cf Ref. [7]. This is true as long as the excitation energies are smaller than energies corresponding to the temperature,  $T = \Delta E$ , i.e. for excitation energies smaller than about  $10 A^{1/3}$  MeV (for  $\varepsilon_2 = 0.25$ ), giving about 30 MeV for mass  $A=25$  and 55 MeV for  $A=160$ . For higher excitation energies a saturation of the rotational enhancement should set in. In this study we concentrate on lower energies, say up to about 10 MeV. It is therefore a reasonable approximation to account for rotational enhancement by simply adding a rotational band on each band head; double-counting of states would not occur.

Rotational states are consequently taken into account by adding a rotational band on top of each intrinsic band-head for deformed nuclei (here defined as nuclei with calculated quadrupole deformation  $|\varepsilon_2| \geq 0.05$ ). The rotational energy of the different angular momentum states,  $I$ , in the rotational band is given by

$$E_{\text{rot}}^i(I, K_i) = \frac{I(I+1) - K_i^2}{2\mathcal{J}_\perp(\varepsilon_2, \Delta_p^i, \Delta_n^i)}, \quad (13)$$

where  $K_i$  is the angular momentum projection on the symmetry axis of the intrinsic state  $i$  upon which the rotational band is built. The quadrupole deformation is denoted by  $\varepsilon_2$  while  $\Delta_p^i$  and  $\Delta_n^i$  denote the proton and neutron pairing gaps of the intrinsic state  $i$ . The moment of inertia around an axis perpendicular to the symmetry axis  $\mathcal{J}_\perp(\varepsilon_2, \Delta_p^i, \Delta_n^i)$  is approximated by the rigid-body moment of inertia with deformation  $\varepsilon_2$ , modified by the calculated pairing gaps for the considered state, as given in Ref. [28]. Given the angular momentum projection  $K$  and parity  $\pi$  of the band-head the rotational band includes the following levels

$$I^\pi = \begin{cases} K^\pi, (K+1)^\pi, (K+2)^\pi, \dots & \text{if } K \neq 0, \\ 0^+, 2^+, 4^+, \dots & \text{if } K = 0^+, \\ 1^-, 3^-, 5^-, \dots & \text{if } K = 0^-. \end{cases} \quad (14)$$

The Coriolis anti-pairing effect is neglected and no virtual crossings of rotational bands are taken into account.

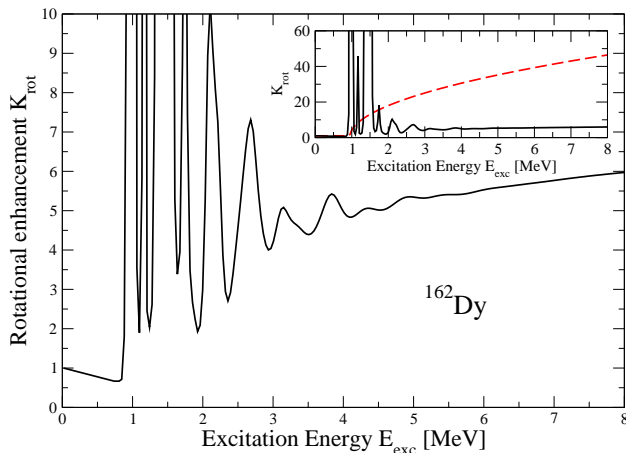


FIG. 1: (Color online) Rotational enhancement,  $K_{\text{rot}}$ , for the nucleus  $^{162}\text{Dy}$  as a function of excitation energy. The insert shows the enhancement compared to the simple enhancement model of Ref. [29] (red dashed line).

Thus, the pairing gap and moment of inertia are assumed to be unchanged from the band-head pairing gap for all states in the rotational band. This approximation is reasonable since mainly low-spin states play a role in the present study.

The total energy of the calculated level is thus given by

$$E_i = E_{\text{mb}}^i + E_{\text{rot}}^i(I, K_i) \quad (15)$$

where  $E_{\text{mb}}^i$  is the energy, Eq. (12), of the intrinsic many-body configuration  $i$ , and  $E_{\text{rot}}^i(I, K_i)$  is the rotation energy, Eq. (13), of the level with angular momentum  $I$  built from the intrinsic many-body configuration with angular momentum projection  $K_i$ . These energies are used to calculate the level density according to Eq. (1).

Fig. 1 shows the rotational enhancement,  $K_{\text{rot}}$ , for the well-deformed nucleus ( $\varepsilon_2=0.26$ )  $^{162}\text{Dy}$  (cf. Fig. 12) calculated as the ratio of the level density when rotations are included or excluded. For low excitation energies there are large fluctuations which are artifacts of the low level density combined with the smoothing procedure of Sec. II E. For higher excitation energies ( $\gtrsim 3$  MeV) the rotational enhancement is a slowly increasing function, of the order of a factor 5 at the neutron separation energy. This prediction is compared to the SU(3) model of Ref. [29], which is shown in the insert of Fig. 1. The SU(3) model gives almost an order of magnitude larger enhancement for excitation energies in the region of the neutron separation energy. We note that a combinatorial level-density model based on the Nilsson potential gives a rotational enhancement for  $^{162}\text{Dy}$  similar to our results [30].

## D. Vibrations

Many nuclei exhibit low-lying states of vibrational character, which are usually of quadrupole or octupole type. Such low-lying vibrational states appear at excitation energies not much lower than the 2qp excitations which in a coherent way build up the collective state. We therefore believe that the vibrational enhancement of the level density, contrary to the rotational enhancement discussed above, must be described microscopically.

In order to describe vibrational states the Quasiparticle-Tamm-Dancoff-Approximation (QTDA) is used. According to the Brink-Axel hypothesis [31, 32] phonons are built on every intrinsic many-body configuration  $E_{\text{mb}}^i$ . The QTDA equation is solved for each state  $i$  in order to get all possible phonon excitation energies and wave-functions. This means solving the QTDA equations millions of times for every single nucleus.

The residual interaction is approximated by the double stretched (isoscalar) Quadrupole-Quadrupole interaction. This interaction is well defined in the case of a harmonic oscillator potential. In the case of a finite-depth potential as the folded-Yukawa potential the interaction should take into account additional finite size effects, for example as is done in Ref. [33]. In the present work the finite-depth effects are ignored and the double stretched approach is used as defined in Refs. [34, 35].

The QTDA secular equation can be written [36]

$$\frac{1}{\chi_{2K}} = \sum_{\mu\nu} \frac{|\langle \mu | \bar{Q}_{2K} | \nu \rangle|^2 (U_\mu V_\nu + V_\mu U_\nu)^2}{(E_\mu^{\text{qp},i} + E_\nu^{\text{qp},i}) - (\hbar\omega)_j^i}, \quad (16)$$

where the effect of Eq. (8) has not been explicitly written out.  $\bar{Q}_{2K}$  is the double stretched quadrupole operator, where the components  $K=0$  and  $K=2$  are considered. The set of roots  $\{(\hbar\omega)_j^i\}$  of this equation is the excitation energies of the vibrational phonons  $j$  on top of the intrinsic state  $i$ , whereas the poles  $E_\mu^{\text{qp},i} = \sqrt{(\epsilon_\mu - \lambda)^2 + \Delta_i^2}$  are the unperturbed two-quasiparticle excitations on the many-body configuration  $E_{\text{mb}}^i$  with pairing gap  $\Delta_i$  as calculated by Eqs. (9) and (10), and  $\epsilon_\mu$  are the single-particle energies.

The self-consistent coupling strength is given by [34]

$$\chi_{2K} = \frac{8\pi}{5} \frac{M\omega_0^2}{A \langle \bar{r}^2 \rangle + g_{2K} \sqrt{\frac{4\pi}{5}} A \langle \bar{Q}_{20} \rangle}, \quad (17)$$

where  $g_{20} = 1$  and  $g_{22} = -1$ . The expectation-values  $\langle \bar{r}^2 \rangle$  and  $\langle \bar{Q}_{20} \rangle$  are calculated in double stretched coordinates [34]. To test that this gives overall reasonable result, we have verified for a large number of nuclei that for the  $K=0$  and the  $K=2$  components of the iso-scalar Giant Quadrupole Resonances the calculations agree well with the systematics of the Giant Resonance energies  $\hbar\omega_{\text{GQR}} = 58A^{-1/3}$  MeV [34].

The phonons are never repeated and double counting is explicitly avoided by the following procedure. The

phonon wave functions are given by

$$\mathcal{O}^\dagger = \sum_{\mu,\nu} X_{\mu,\nu} a_\mu^\dagger a_\nu, \quad (18)$$

where  $X_{\mu,\nu}$  are the wave-function components of all excited quasi-particle states  $a_\mu^\dagger a_\nu$  on top of the configuration  $E_{\text{mb}}^i$ . The level density is increased by one state at the energy of the phonon  $(\hbar\omega)_j^i$ , and decreased by the amount given by the wave-function component  $X_{\mu,\nu}^2$  at the energy of the corresponding pole  $(E_\mu^{\text{qp},i} + E_\nu^{\text{qp},i})$ . The change in level density due to the phonon  $j$  on top of intrinsic state  $i$  is thus

$$\delta\rho(E) = \delta(E - E_{\text{mb}}^i - (\hbar\omega)_j^i) - \sum_{\mu,\nu} X_{\mu,\nu}^2 \delta(E - E_{\text{mb}}^i - (E_\mu^{\text{qp},i} + E_\nu^{\text{qp},i})), \quad (19)$$

where  $E$  is the excitation energy relative to the ground-state. This procedure increases the level density by reducing the strength of the pure quasi-particle excitations and adding strength by means of the phonons (which are pushed down in energy due to the  $QQ$ -interaction).

Most phonons have little collectivity in the QTDA approximation, as most of the phonon excitations lie very close to a pure quasi-particle excitation, and hence the wave-function is completely dominated by that single component. Even if there are a few very collective low-lying phonon states the vibrational enhancement of the level density becomes small, since most excited states provide quite non-collective phonon excitations. Due to this non-collectivity of most phonons there is no way that the phonons, in general, can be repeated to form two- or even three-phonon excitations.

The vibrational enhancement factor in this method is in general quite small, of the order of a few percent. This is substantially lower than predictions from other models. For example, the attenuated phonon method [12, 14, 37] and the Boson partition function method [38] both give up to an order of magnitude enhancement at the neutron separation energy. Fig. 2 shows the vibrational enhancement as a function of excitation energy for  $^{162}\text{Dy}$ . The effect is very small, close to 1 % at 7 MeV excitation energy. For the same nucleus the attenuated phonon method gives an enhancement factor of about 3 as shown in the insert of Fig. 2.

The level-density enhancement due to quadrupole vibrations is thus found to be very small. Higher multipole vibrations (as octupole vibrations) are expected to contribute with enhancements of the same order of magnitude or less and are neglected in the CFY model.

### E. Many-body damping width

In the mean-field approach all excited many-body states are treated as non-interacting. A residual two-body interaction will mix the many-body states obtained

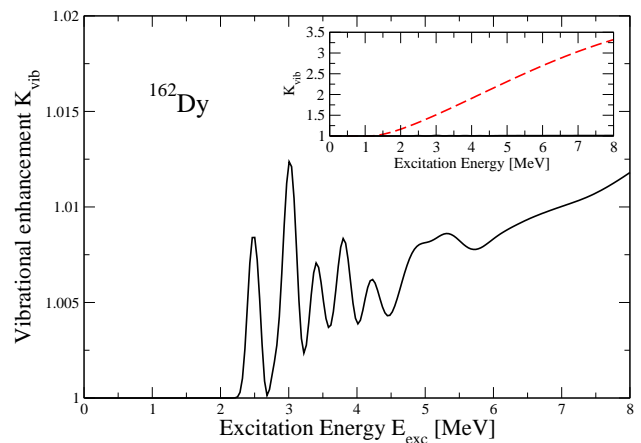


FIG. 2: (Color online) Vibrational enhancement,  $K_{\text{vib}}$ , using the QTDA method for the nucleus  $^{162}\text{Dy}$  as a function of excitation energy. The insert shows the enhancement compared to the enhancement of the attenuated phonon model of Ref. [12] (red dashed line).

from the combinatorics. Smearing effects from the residual interaction can approximately be taken into account by assuming a spreading width of all excited states. The spreading width is implemented in terms of a Gaussian envelope with width  $\sigma$ , i.e. the delta functions in Eq. 1 are replaced by Gaussians. Estimates of the spreading width FWHM gives [39]

$$\Gamma = 0.039 \left( \frac{A}{160} \right)^{-1/2} E^{3/2} \text{ MeV}, \quad (20)$$

where the FWHM is related to the Gaussian spreading width  $\sigma = \frac{\Gamma}{2\sqrt{2\ln 2}}$ .

Assuming that all excited many-body states in an energy bin  $\Delta E$  are uniformly distributed, the level density becomes

$$\rho(E_b) = \sum_a \rho(E_a) \frac{1}{2} \left[ \text{erf} \left( \frac{E_a + \Delta E/2 - E_b}{\sqrt{2}\sigma} \right) - \text{erf} \left( \frac{E_a - \Delta E/2 - E_b}{\sqrt{2}\sigma} \right) \right], \quad (21)$$

for bin-point  $b$ . The method implies a smearing out of level-density properties over a range  $\Gamma$ , which is smoothly increasing with excitation energy. As a consequence fluctuations of energies and wave-functions in the range  $\Gamma$  follow GOE statistics of Random Matrix theory, that is often denoted as quantum chaos in the nucleus, see e.g Refs. [40, 41].

### III. LEVEL DISTRIBUTIONS

In the present combinatorial approach it is possible to extract different distributions exhibiting details of the level-density function. We present here microscopically

calculated distributions for pairing gaps (Sec. III A), parity (Sec. III B), and angular momentum (Sec. III C).

### A. Pairing-gap distribution

The BCS equations, Eqs. (9) and (10), are solved for all individual many-body configurations and hence pairing gaps for all states are obtained. In Fig. 3 the distribution of proton pairing gaps for  $^{162}\text{Dy}$  is shown for a number of excitation energies. For the lowest excitation energies only the ground-state and the states in the ground-state rotational band exist. The pairing gap of the levels in the rotational band is fixed to be the same as the pairing gap of the band-head, see Sec. II C. As the excitation energy increases levels with reduced pairing gaps appear. However, no transition to a completely unpaired system is observed, and levels with non-collapsed gaps ( $\Delta > 0$ ) survive to the highest considered excitation energies. At the highest considered excitation energy for  $^{162}\text{Dy}$ ,  $E_{\text{exc}} = 8.4$  MeV, 36% of the levels still have a non-zero proton pairing gap, see Fig. 3. The mean value of the proton pairing gap  $\langle \Delta \rangle$  at different excitation energies is shown in Fig. 4 for  $^{162}\text{Dy}$ . Between 2 MeV and 3.5 MeV excitation energy there is a rapid decrease in the mean pairing gap. At higher excitation energies the decrease is slower. At 8.4 MeV excitation energy the mean value is  $\langle \Delta \rangle = 0.2$  MeV. The reason why pairing may survive and be of substantial size in states at these high energies can be explained as follows: Several highly excited states are built by exciting particles and holes far from the Fermi energy, where blocking in the BCS equations has no effect on the pairing gap.

The non-collapsed pairing gaps influence the moment of inertia and keep it reduced as compared to the rigid-body value. This implies that even at excitation energies in the region of the neutron separation energy the moment of inertia is on average smaller than the rigid-body value. A similar observation is made in Ref. [15].

### B. Parity distribution

In Fermi-gas level-density models there is an implicit assumption of equal number of states with different parity at any given excitation energy. However, models that take into account microscopic effects show clear structure in the parity ratio, see eg. Refs. [16, 42, 43]. In connection with astrophysical reaction rates the parity ratio may play an important role, and can be included in the Hauser Feshbach formalism, see eg Refs. [44, 45].

From the single-particle point of view it is clear that the parity ratio should show structure. For  $^{84}_{38}\text{Sr}_{46}$  the situation is illuminating. The nucleus is close to spherical in its ground-state ( $\varepsilon_2 = 0.05$ ) [21]. It has 2 proton holes in the  $pf$  shell and 6 neutrons in the  $g_{9/2}$  shell. Since there are large gaps in the single-particle spectrum the energy to excite nucleons across the gaps, which cause changes

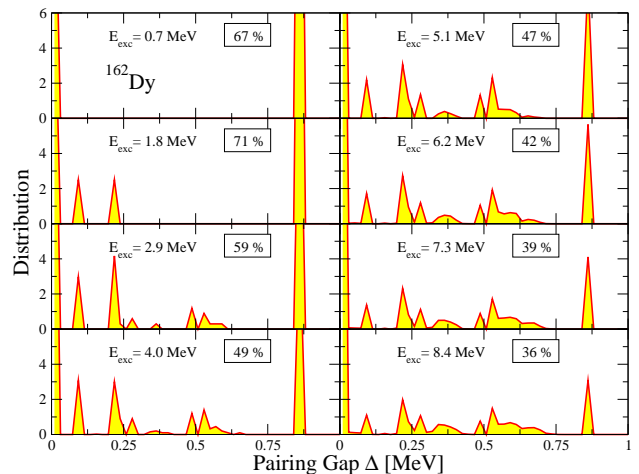


FIG. 3: (Color online) Proton pairing-gap distributions at different excitation energies  $E_{\text{exc}}$  for  $^{162}\text{Dy}$  shown in 20 keV pairing-gap bins. The proportion of paired states ( $\Delta > 0$ ) are shown in percent in the boxes.

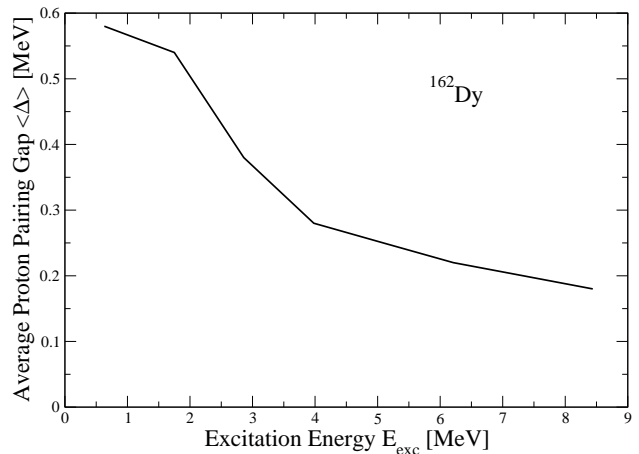


FIG. 4: Average proton pairing gap  $\langle \Delta \rangle$  at different excitation energies  $E_{\text{exc}}$  for  $^{162}\text{Dy}$ . The mean values are given by the distributions in Fig. 3.

in parity, is quite large. The parity ratio displays long-range oscillations, see upper left panel of Fig. 5, which are directly connected to the large single-particle gaps. The single-particle gaps effectively decrease with increasing deformation, and the oscillations are therefore expected to decrease with deformation. To test these ideas the parity ratio in  $^{84}\text{Sr}$  is calculated at different deformations and shown in Fig. 5. Indeed, for larger deformations the oscillatory pattern vanishes and the parity ratio equilibrates to one.

In Fig. 6 the parity ratios for  $^{56}\text{Fe}$ ,  $^{60}\text{Ni}$  and  $^{68}\text{Zn}$  are shown and compared to two calculations of Ref. [16]. The solid blue lines show the CFY model, the red dashed lines show the statistical parity projection model and the black dots show calculations using the Shell-Model Monte-Carlo method. The parity ratio in the Fe and

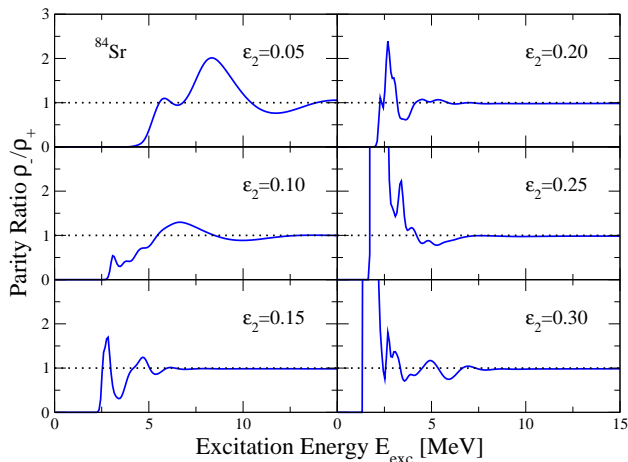


FIG. 5: (Color online) Parity ratio versus excitation energy for  $^{84}\text{Sr}$  calculated with different deformations. Large deformations imply a parity distribution close to 1 even at low excitation energies. For small deformations the parity non-equilibrium can survive to high excitation energies.

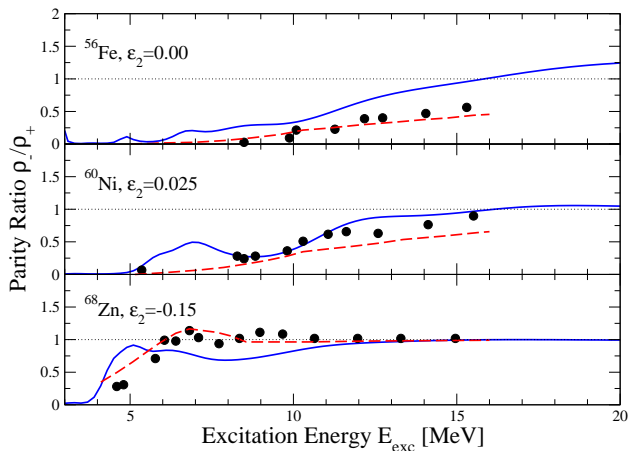


FIG. 6: (Color online) Parity ratio versus excitation energy. The solid blue lines are calculated with the CFY model. The red dashed line and black dots are given by a statistical model and a Monte-Carlo method, respectively [16].

Ni isotopes is not equilibrated below 15 MeV in any of the calculations, while  $^{68}\text{Zn}$  equilibrates at much lower energies (below 10 MeV). For  $^{60}\text{Ni}$  and  $^{68}\text{Zn}$  there is a clear oscillatory behavior prior to equilibration in the CFY model, and in the case of Ni there is a good agreement between the Monte-Carlo method and the CFY model, especially in the region of 8–12 MeV excitation energy. Note, however, that fluctuations seen in the present micro-canonical approach may be smeared out by the grand-canonical approach as used in Ref. [16].

The parity ratio has been calculated for Sr-isotopes within a statistical method in Ref. [45] where the impact on astrophysical reaction rates was investigated and found to be small. The statistical method gives at most one oscillatory maximum before it equilibrates, as seen in

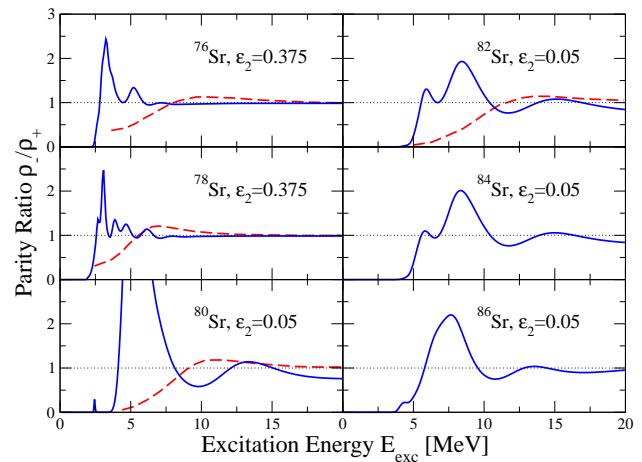


FIG. 7: (Color online) Parity ratio versus excitation energy for Sr isotopes. The solid blue lines are obtained from the CFY model and the dashed red lines are obtained from the statistical parity projection of Ref. [45].

Fig. 7 (dashed lines). In the CFY model the parity ratio has substantially more structure (solid lines). Nuclei with small ground-state deformations show long-range oscillations which survive to high excitation energies before equilibration. The overall results are quite different from the model of Ref. [45].

### C. Angular momentum distribution

In Fermi-gas models the distribution of angular momentum is given by the Gaussian envelope in the spin cutoff model, see eg. Ref. [4],

$$\mathcal{F}(U, I) = \frac{2I+1}{2\sigma^2} \exp\left(\frac{-I(I+1)}{2\sigma^2}\right), \quad (22)$$

which is obtained by random coupling of uncorrelated spins of the nucleons. In Eq.(22) the spin cutoff factor,  $\sigma$ , is defined by

$$\sigma^2 = \frac{\mathcal{J}_{\text{rigid}}}{\hbar^2} \sqrt{\frac{U}{a}}, \quad (23)$$

where  $\mathcal{J}_{\text{rigid}}$  is the rigid-body moment of inertia,  $U = E - \delta$  is the effective excitation energy shifted by the back-shift  $\delta$ , and  $a$  is the level-density parameter.

In Fig. 8 the angular-momentum distributions for  $^{68}\text{Zn}$  and  $^{162}\text{Dy}$  are shown for several excitation-energy regions. The black lines with dots show the CFY model results while the red solid lines show the Gaussian distribution of Eq. (22) with the spin cutoff factors given in Ref. [4], and the blue dashed lines show Gaussian distributions fitted to the combinatorial calculation. For low excitation energies there are clear deviations from the Gaussian profiles while for higher excitations the combinatorial distribution tends to the Gaussian profile. However, for  $^{68}\text{Zn}$  the deviations from a Gaussian angular

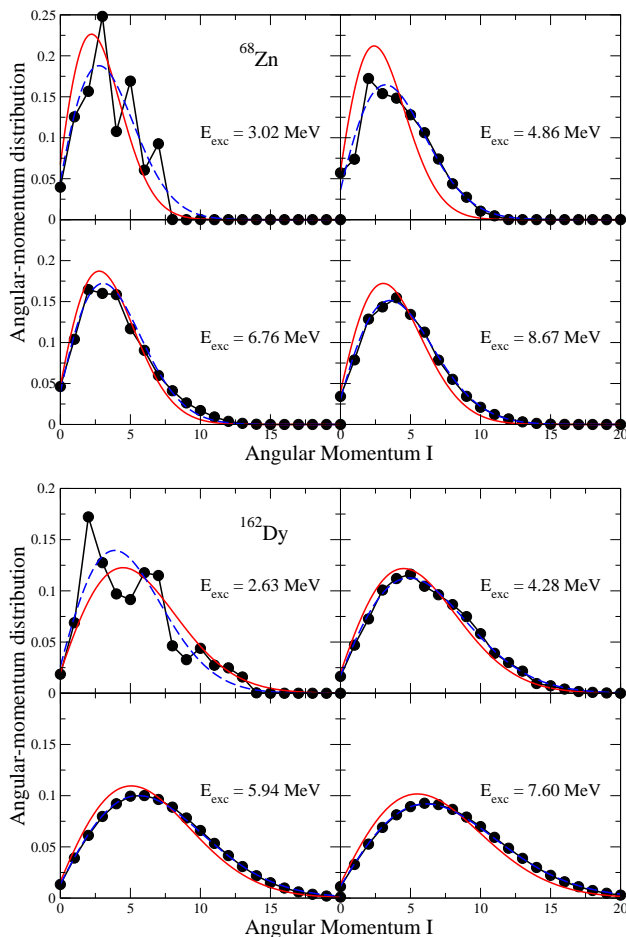


FIG. 8: (Color online) Angular-momentum distribution for  $^{68}\text{Zn}$  and  $^{162}\text{Dy}$  in 4 different excitation-energy regions. The black lines with dots show results from the CFY model. The red solid lines and blue dashed lines show the Gaussians given by Eq. (22) using the spin cutoff factors from Ref. [4] and a direct fit to CFY, respectively.

momentum distribution remain up to about the neutron separation energy ( $S_n=6.48$  MeV).

For low excitation energies in  $^{68}\text{Zn}$  there is an odd-even spin staggering which is not explained by the spin cutoff model. This effect has also been observed in Fe-isotopes in the Shell Model Monte-Carlo Method [17].

Fig. 9 shows the spin cutoff factor deduced from the CFY model (black solid line) and from the statistical model [4] (red dashed line), as a function of excitation energy for  $^{162}\text{Dy}$ . For this particular nucleus the spin cutoff factor for excitation energies  $\gtrsim 3$  MeV is similar in shape but  $\sim 10\%$  larger than in the statistical model [4]. The fact that the statistical model is smaller than the CFY model, despite the presence of pairing in the CFY model, is accidental for this nucleus. Since both the rigid body moment of inertia and the level density parameter are fitted to experiments using only three parameter, the detailed description for a particular nucleus might give this result when compared to a very different model as

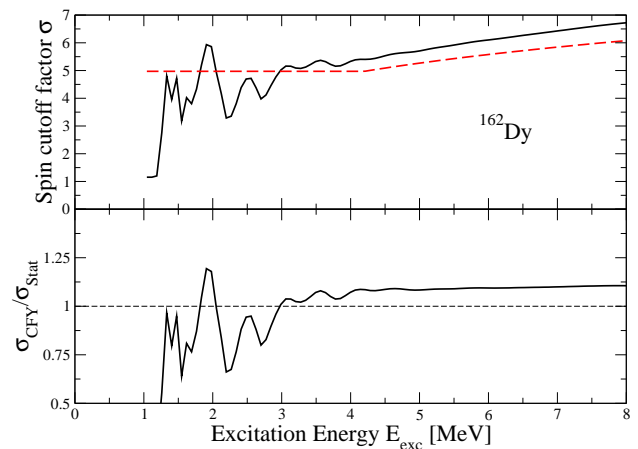


FIG. 9: (Color online) The top panel shows the spin cutoff factor as a function of excitation energy for  $^{162}\text{Dy}$  in the CFY model (black solid line) and the statistical model of Ref. [4] (red dashed line). The bottom panel shows the ratio of the combinatorial and statistical spin cutoff factors of the top panel.

the CFY model.

#### IV. COMPARISON WITH EXPERIMENTAL DATA

##### A. Neutron separation-energy level spacings

The s-wave neutron resonance spacings constitute the most comprehensive experimental database for comparison with NLD calculations [46]. This database serves as a benchmark for all large-scale level-density models [4, 14, 15, 47].

The s-wave neutron resonance spacing  $D_0$  at the neutron separation energy  $S_n$  of the compound nucleus ( $Z, N$ ) is obtained from calculated level densities  $\rho(E, I, \pi)$  as,

$$\frac{1}{D_0} = \begin{cases} \rho(S_n, I_0 + 1/2, \pi_0) + \rho(S_n, I_0 - 1/2, \pi_0) & \text{for } I_0 > 0, \\ \rho(S_n, 1/2, \pi_0) & \text{for } I_0 = 0, \end{cases} \quad (24)$$

where  $I_0$  is the ground-state spin and  $\pi_0$  is the ground-state parity of the target nucleus ( $Z, N - 1$ ). In Fig. 10 we study the ratio of calculated and experimental level spacings at the neutron separation energy,  $D_{\text{Th}}/D_{\text{Exp}}$ , for all nuclei in the database.

The quality of a level-density model can be estimated by the rms-factor [15]

$$f_{\text{rms}} = \exp \left[ \frac{1}{N_e} \sum_{i=1}^{N_e} \ln^2 \frac{D_{\text{Th}}^i}{D_{\text{Exp}}^i} \right]^{1/2}, \quad (25)$$



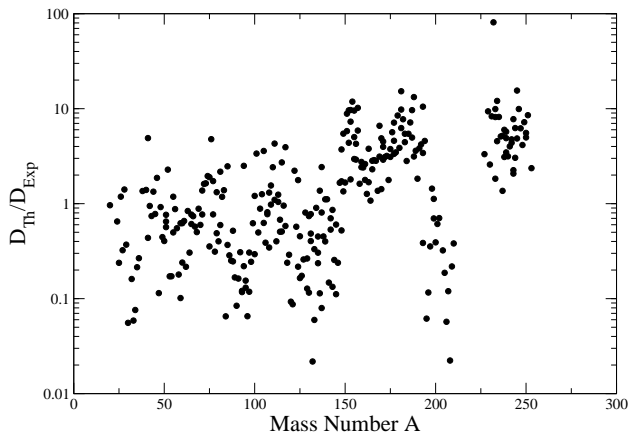


FIG. 10: Ratio between theoretical and experimental level spacings at neutron separation energy versus mass number  $A$ . The rms-factor is  $f_{\text{rms}} = 4.2$ . The experimental data are taken from Ref. [46].

and the mean factor

$$m = \exp \left[ \frac{1}{N_e} \sum_{i=1}^{N_e} \ln \frac{D_{\text{Th}}^i}{D_{\text{Exp}}^i} \right], \quad (26)$$

where  $D_{\text{Th}}^i$  and  $D_{\text{Exp}}^i$  are the theoretical and experimental level spacings and  $N_e$  is the number of nuclei in the database. The CFY model gives  $f_{\text{rms}} = 4.2$  and  $m = 1.1$ , see Fig. 10 of the error ratio versus  $A$ . These results are compared to other statistical and combinatorial models in Table II and discussed in Sec. V.

There seems to be a clear residual shell structure in the level spacings, as seen in Fig. 10, especially in the doubly magic  $^{208}\text{Pb}$  region. A similar effect can be observed for the Gogny model in Ref. [15], and in results of the Skyrme model with the BSk9 interaction, as shown in Ref. [14]. In addition, there seems to be a drift with mass number where especially nuclei in the rare-earth and actinide regions over-estimate the neutron separation level spacings. A similar drift can be seen in the Gogny model of Ref. [15] while it seems not to be present in the Skyrme-HFB model in Ref. [14].

The rare-earth and actinide regions, where too large level spacings are calculated, mainly correspond to deformed nuclei. On the other hand, nuclei corresponding to regions with particularly low ratio  $D_{\text{Th}}/D_{\text{Exp}}$  seen in Fig. 10 (around  $A=32$ , 132 and 208) correspond to spherical nuclei. The overestimation of  $D$  for deformed nuclei (too low calculated level density), and underestimation of  $D$  for spherical nuclei (too high calculated level density) seems to be approximately systematic, as seen in Fig. 11, where the ratio between theoretical and experimental level spacings is shown versus the absolute value of the deformation.

However, as seen in the lower panel of Fig. 11 there is no clear correlation with the microscopic energy  $E_{\text{mic}}$  of Ref. [21] as might be expected from the residual shell structure seen in Fig. 10.

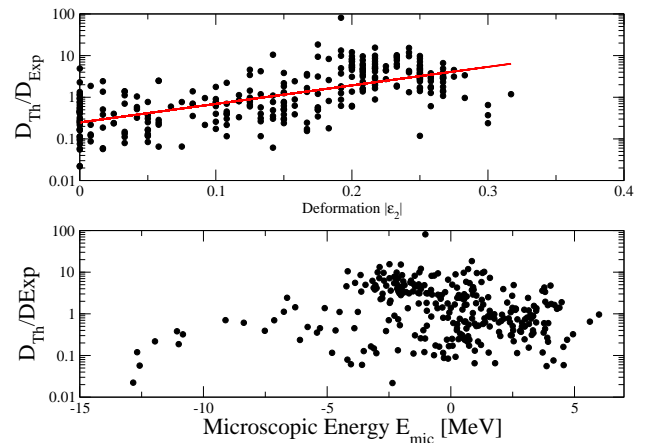


FIG. 11: (Color online) The top panel shows the ratio between theoretical and experimental level spacings at neutron separation energy versus the absolute value  $|\epsilon_2|$  of the calculated quadrupole deformation. The bottom panel shows this ratio as a function of the microscopic energy. The solid red line shows an exponential fit to illustrate the correlation. The microscopic energies and the quadrupole deformations are taken from Ref. [21]. The experimental data are from Ref. [46].

## B. Detailed level-density functions

The Oslo method is a commonly used experimental method for extracting detailed level-density functions for large ranges of excitation energy [19]. It provides a valuable test for NLD models. However, the approach is model dependent since the level density is extracted by use of a back-shifted Fermi Gas approximation and a spin-cutoff factor, see also discussion in Ref. [38].

In Figs. 12 and 13 level densities obtained from the CFY model are compared to data for a number of nuclei where experimental data are available [48, 49, 50, 51, 52, 53].

In Fig. 12 we show level densities of the rare-earth nuclei  $^{148,149}\text{Sm}$ ,  $^{161,162}\text{Dy}$ ,  $^{166,167}\text{Er}$ , and  $^{170,171,172}\text{Yb}$  as functions of excitation energy. The data are in general well reproduced by the CFY model, with an error of less than a factor of 2. The good agreement between the calculated and experimental slopes indicates that the single-particle structure and the moments of inertia in the rotational bands are sound. However, an observable trend in this mass region is that the level density for even-even nuclei is slightly over-estimated and for odd nuclei the level density is slightly under-estimated. The effective back-shift is to a large extent controlled by the ground-state pairing gap. By fine-tuning the pairing gaps it is possible to get an almost perfect agreement with experiment. However, in this paper no efforts are made to adjust parameters of the model to fit measured level-density data. Indeed, the ground-state pairing gaps are given by the mass model, see Sec. II B. Neither are any renormalizations of calculated level densities to fit data performed, as is sometimes done in other models, see Refs. [14, 38].

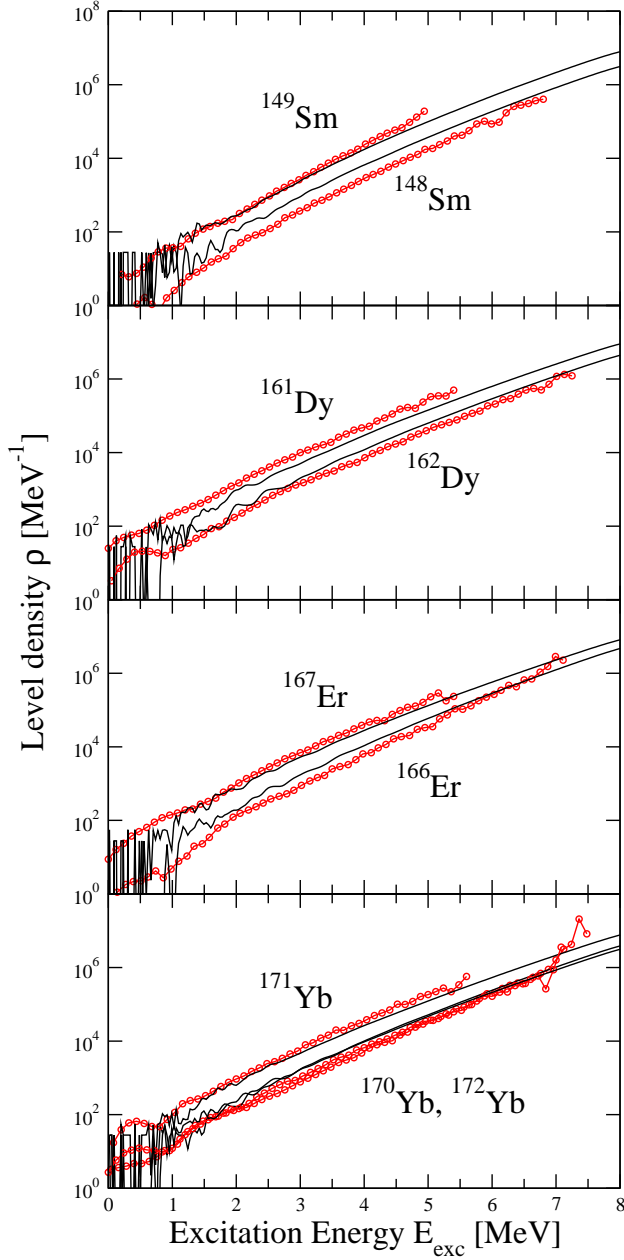


FIG. 12: (Color online) Level densities  $\rho$  as functions of excitation energy for Sm, Dy, Er and Yb isotopes. The black solid lines show the CFY model and the red dots show the experimental data [50, 51, 52, 53].

Experimental level-density functions are available also for lighter mass regions, and in Fig. 13 data for V and Mo isotopes are shown. The overall agreement between the model and these experimental data is somewhat inferior to what was obtained in the rare-earth region. For the Mo isotopes in Fig. 13 the CFY model is roughly a factor of 3 too large for high excitation energies while for the V isotopes the over-estimation is roughly a factor of 4. However, these errors are consistent with the overall results from the neutron separation level spac-

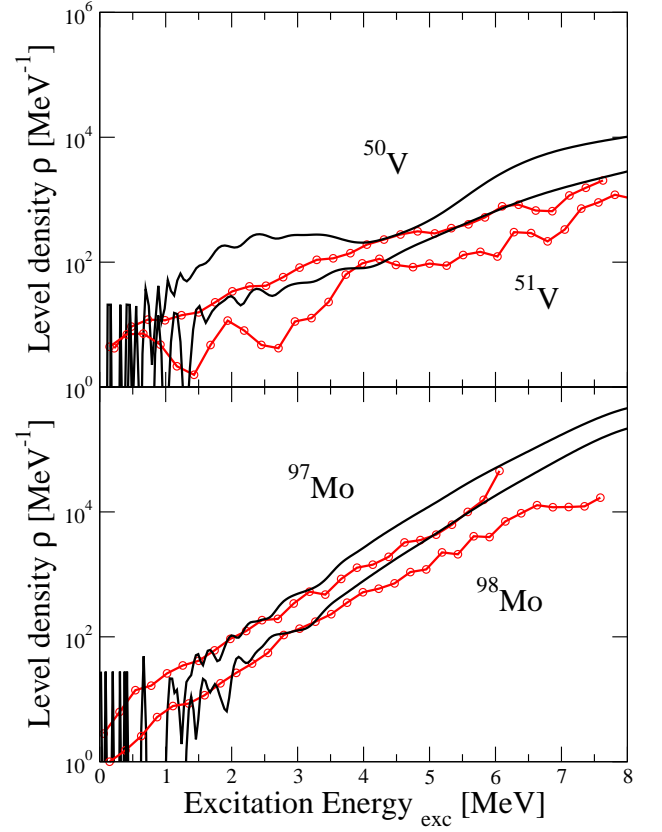


FIG. 13: (Color online) Level densities as functions of excitation energy for  $^{50,51}\text{V}$  and  $^{97,98}\text{Mo}$ . The black solid lines show the CFY model and the red dots show the experimental data [48, 49].

ing, see Fig. 10, which have an overall  $f_{\text{rms}} = 4.2$ . Also, the slopes and the detailed structures are not as well described in these nuclei as in the rare-earths. Especially  $^{50}\text{V}$  exhibits an oscillatory pattern in the CFY model, which is an effect of the small ground-state deformation  $\varepsilon_2 = 0.05$  [21]. A corresponding oscillatory pattern is not as clearly present in the experimental data. In  $^{51}\text{V}$  the experimental data shows oscillatory behavior while the CFY model is more smooth. The ground-state deformation is slightly larger with  $\varepsilon_2 = 0.083$  [21], which in the CFY model means that since the moment of inertia is larger the rotational states have a larger influence and smooths the level density.

### C. Low-lying discrete levels

The amount of experimental information on low-lying discrete energy levels is indeed substantial. In addition to the energy parity and angular momentum are often known. In Ref. [22] a global comparison is made between measured and FRLDM calculated ground-state spins and parities for odd-mass nuclei, and the agreement was found to be very good. The collection of low-energy data

provides important information for level-density models, since the accuracy of the model can be studied at the very lowest energies. Cumulative distributions of known levels can thus be constructed, and compared to calculations. In Ref. [14] a selection of 15 different nuclei was made to represent all different kinds of nuclear aspects, such as light-heavy, spherical-transitional-deformed, as well as odd-odd, even-even and odd-even nuclei (also used in Ref. [38]). We therefore compare our model low-lying level densities to experimental data for the identical set of 15 nuclei.

The cumulative level density for the 15 nuclei are shown in Fig. 14. The CFY model (solid blue line) is compared to experimental data (black dash-dotted line) and to the HFB model (red dashed line) of Ref. [38]. For a good agreement with data, the calculated line should follow as precise as possible the experimental curve at the lowest energies, and should then smoothly deviate, always larger than data.

In general, the theoretical models seem to give very comparable results for deformed nuclei while differences are larger for transitional and spherical nuclei. For the light spherical nuclei, like  $^{42}\text{K}$  and  $^{56}\text{Fe}$  there are pronounced single-particle gap effects which cause jumps in the level density. These effects are smoothly disappearing at higher energies. A quite drastic deviation between our calculation and data is seen for  $^{208}\text{Pb}$ . The calculated (cumulative) level density is systematically larger starting already at about 3 MeV excitation energy (in the figure seen at 0.5 MeV; the energy scale is shifted by 2.5 MeV for this nucleus). This is also seen in the total level density at the neutron separation energy, and in Table I the ratio between theoretical and measured level spacings at the neutron separation energy is listed for the 9 nuclei. For  $^{208}\text{Pb}$  this ratio is 0.02, i.e. the calculated level density is about 50 times larger than experiment!

When comparing to the HFB model calculation of the level density [38] one should note that interpolations between different deformations are included in this model, while in our model the ground-state deformation is kept fixed for all excited states. In particular, this somewhat phenomenological way to treat deformation changes has strong effects on the results for  $^{127}\text{Te}$ .

Nucl	$D_{\text{Th}}/D_{\text{Exp}}$	Nucl	$D_{\text{Th}}/D_{\text{Exp}}$	Nucl	$D_{\text{Th}}/D_{\text{Exp}}$
$^{42}\text{K}$	0.94	$^{56}\text{Fe}$	0.55	$^{60}\text{Co}$	0.62
$^{94}\text{Nb}$	2.50	$^{107}\text{Cd}$	0.77	$^{127}\text{Te}$	0.26
$^{148}\text{Pm}$	1.72	$^{155}\text{Eu}$	2.95	$^{161}\text{Dy}$	2.61
$^{162}\text{Dy}$	1.27	$^{172}\text{Yb}$	3.10	$^{194}\text{Ir}$	4.58
$^{208}\text{Pb}$	0.02	$^{237}\text{U}$	5.18	$^{239}\text{Pu}$	3.46

TABLE I: Table of neutron separation energy spacings compared to experimental data for the nuclei showed in Fig. 14.

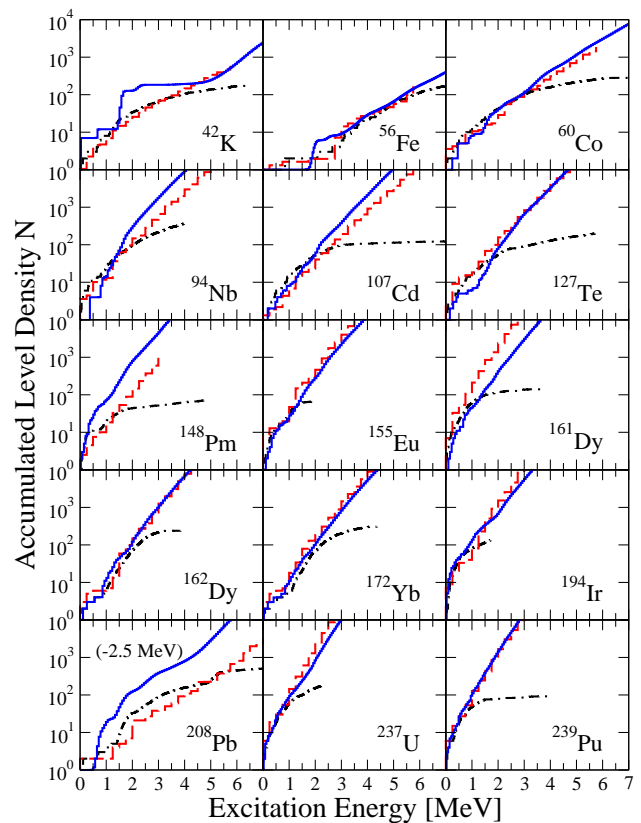


FIG. 14: (Color online) Accumulated level density as a function of excitation energy. The blue solid and red dashed lines show the present CFY model and the HFB model [38]. The black dash-dotted line shows experimental data collected in Ref. [38].

#### D. Parity ratio

The parity ratio has been measured experimentally by Kalmykov et.al. [20] for the two spherical nuclei  $^{58}\text{Ni}$  and  $^{90}\text{Zr}$ . For these nuclei the  $I = 2$  angular-momentum component of the level density is measured and separated into parity components. In the top panel of Fig. 15(a) the level-density component  $\rho(E, I = 2, \pi = \pm 1)$  for  $^{90}\text{Zr}$  is compared to CFY model calculations. The level densities from the CFY model are in good agreement with experimental data, and in the lower panel of Fig. 15(a) the parity ratio is shown. Predictions for the total level density as well as the  $I = 2$  component are shown as black solid and red dashed lines, respectively. The difference between the parity ratio for the total level density and the  $I = 2$  component decreases with excitation energy, because the spin cutoff model becomes more realistic when the excitation energy increases, see Sec. III C. For the parity ratio the CFY model result is within the experimental error-bars for all excitation energies and seems to show a similar pattern as the experiments: a high parity ratio (excess of negative parity states) at 8 MeV and a low ratio (excess of positive parity states) at 11 MeV excitation energy. The blue dot-dashed line shows the

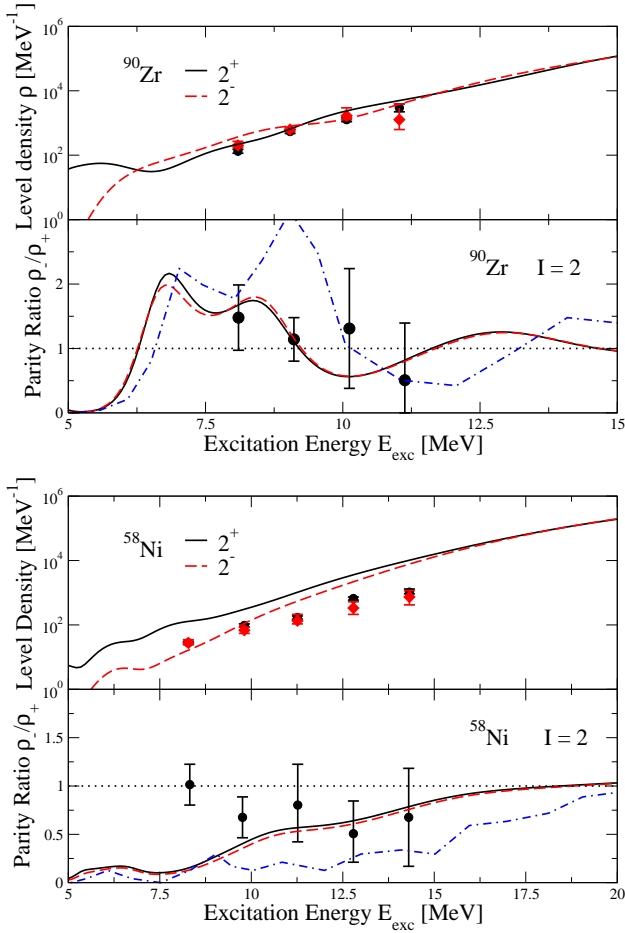


FIG. 15: (Color online) The top panels show CFY calculated components of the  $2^+$  (black solid) and  $2^-$  (red dashed) level densities for  $^{90}\text{Zr}$  (top part of figure) and  $^{58}\text{Ni}$  (lower part of figure), as functions of excitation energy. Experimental data from Ref. [20] are shown as black dots and red diamonds with error-bars for  $2^+$  and  $2^-$ , respectively. The lower panels show for each nucleus the parity ratio versus excitation energy. The solid black and dashed red lines show the CFY model results for the total level density and the  $I=2$  component, respectively. The blue dot-dashed lines show the Skyrme-HFB model of Ref. [14]. Experimental data from Ref. [20] are shown with error-bars.

Skyrme-HFB model of Ref. [14]. It is also within the experimental error-bars for all excitation energies except at 9 MeV where the HFB model gives a large positive ratio ( $\sim 3$ ) while the experiments and the CFY model are close to unity.

The  $I = 2$  component of the level density in  $^{58}\text{Ni}$  is shown in the top panel of Fig. 15(b). The agreement between experimental data and the CFY model is somewhat inferior to what we obtained for  $^{90}\text{Zr}$ . For both parities the level density seems to increase faster in the CFY model than what is seen in the experimental data. At 14 MeV excitation energy the model overestimates the level density by roughly a factor of 6. The parity ratio is shown in the lower panel of Fig. 15(b). The ex-

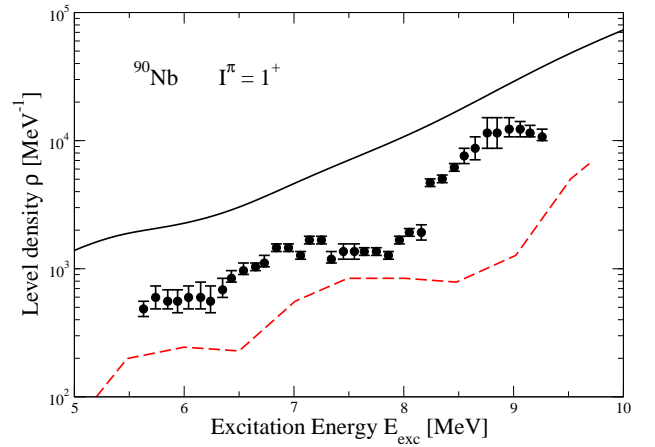


FIG. 16: (Color online) Level density of the  $1^+$  component of the level density as a function of excitation energy for  $^{90}\text{Nb}$ . The black solid and red dashed lines show the CFY model and Skyrme-HFB model of Ref. [14], respectively. Data from Ref. [20] are shown as black dots with error-bars.

perimental parity ratio is close to unity at 8 MeV and then decreases with increasing excitation energy. The CFY model shows a different pattern. It gives a very low parity ratio at low excitation energies with an almost monotonic increase with increasing excitation energy. The ratio only becomes close to unity at 20 MeV. The Skyrme-HFB model of Ref. [14] shows a similar pattern as the CFY model but with an even lower ratio for excitation energies below 20 MeV.

The  $1^+$  component of the level density of  $^{90}\text{Nb}$  has also been measured in Ref. [20]. Fig. 16 shows the experimental data compared to the CFY and Skyrme-HFB models. In the experimental data there is a clear oscillating structure. The CFY model (black solid line) over-estimates the level density and the oscillating structure is much less pronounced. In the Skyrme-HFB model (red dashed line) there are long-range oscillations similar to what is seen in the experimental data, but the energy separation between consecutive minima is larger. The level density is under-estimated in the Skyrme-HFB model, whereas the CFY model over-estimates the level density by a similar factor.

## V. COMPARISON WITH OTHER MODELS

The CFY model is here compared to other statistical and combinatorial NLD models that provide neutron resonance level spacings. In general, the statistical models listed in Table II have an rms deviation just below 2. This low rms deviation is obtained because several parameters in the level-density formulas are directly adjusted to the neutron separation-energy level spacings and low-lying discrete energy levels.

The back-shifted Fermi model of Ref. [47] is based on a simple Fermi-gas formula whereas the Constant Tem-

Statistical Models	$f_{\text{rms}}$	Ref.
Back-shifted Fermi Model	1.71	[47]
Const. Temp. Model	1.77	[47]
Back-shifted Fermi + Const. Temp. Model	1.7	[4]
Generalized Superfluid Model	1.94	[47]
Combinatorial Models	$f_{\text{rms}}$	Ref.
Skyrme-HFB	2.35	[47]
Gogny-HFB	4.55	[15]
CFY	4.2	Present

TABLE II: Table of rms-factors  $f_{\text{rms}}$  for statistical and combinatorial models for neutron separation energy level spacings [4, 15, 47].

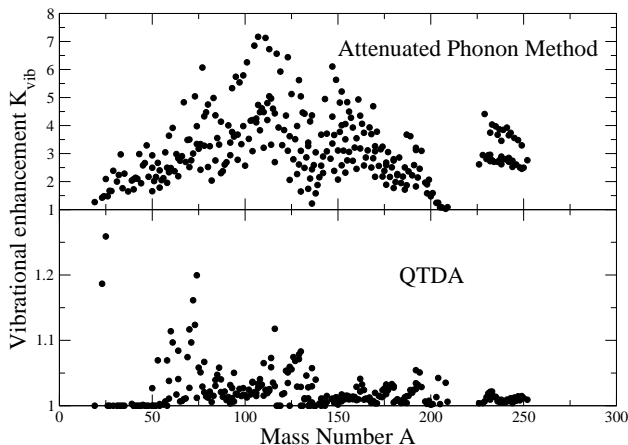


FIG. 17: Vibrational enhancements at the neutron separation energy in the attenuated phonon method (top panel) and the QTDA method (bottom panel) versus of mass number  $A$ .

perature model is based on the approach of Gilbert and Cameron [10]. Both models contain explicit enhancement factors for rotations and vibrations. The model by Rauscher, Thielemann and Kratz [4] is also based on the approach of Gilbert and Cameron. In contrast to the first two models this model has no explicit enhancement factors for rotations and vibrations. It accounts for shell effects and thermal damping in terms of an effective level-density parameter. The model uses the microscopic energy corrections of Ref. [21] together with three free parameters in the fitting procedure. The Generalized Superfluid Model is similar to the models mentioned above. In addition it takes into account how pairing evolves with increasing excitation energy. It also incorporates explicit rotational and vibrational enhancements [47].

Predictions by statistical models in regions outside the fitting region probably give much less accurate results than in the adjustment region. On the other hand, since the combinatorial models are all based on calculated single-particle spectra they could in principle have better predictive power, in particular in regions where

the single-particle model is sound. In contrast, they are not equally flexible in terms of parameter fits to the level spacings database. Therefore, the rms deviation factor of combinatorial models with respect to known data is larger than for the statistical models. The  $f_{\text{rms}} = 4.2$  for the CFY model is about a factor of 2 larger than in statistical models. However, the latter result is obtained with *no* parameters specifically fitted to the level-density data. The mean deviation factor  $m = 1.1$  indicates that the level density is on average reasonable. However, there seems to be a drift with mass number, as seen in Fig. 10, present in the CFY model which is not seen in the HFB models of Refs. [15, 47].

In the lower part of Table II the CFY model is compared to two other large-scale combinatorial NLD models based on the HFB method. The model of Ref. [15] is based on the Gogny D1S interaction for the mean-field and incorporates combinatorial rotations (similar to Sec. II C but no pairing dependence of the moment of inertia), and the attenuated phonon method is applied to account for vibrational states. Pairing is included explicitly for the ground-state, and excited states are back-shifted by an energy-dependent gap procedure. The model gives  $f_{\text{rms}} = 4.55$  for the subset of even-even axially deformed nuclei. The error is slightly larger than the CFY model.

For the Skyrme-HFB NLD model the deviation factor is  $f_{\text{rms}} = 2.35$  [47], which is  $\sim 35\%$  larger than the statistical models and 44% smaller than in the CFY model. This model is based on a Skyrme-HFB mean-field together with combinatorial rotations and the attenuated phonon method for modeling vibrational states. In addition a phenomenological deformation change from deformed to spherical shape at some specified excitation energy is incorporated.

The attenuated phonon method is a phenomenological way to model nuclear vibrations, see eg. Refs. [12, 14]. It assumes that the quadrupole and octupole phonon states in nuclei can be modeled by a gas of non-interacting bosons. The vibrational excitation energies are taken from systematics of the lowest non-rotational  $2^+$  and  $3^-$  states. The model is formulated as a multiplicative factor  $K_{\text{vibr}} = \exp[\delta S - \delta U/T]$  which enhances the level density.  $T$  is the nuclear temperature and the  $\delta S$  and  $\delta U$  are the entropy and internal energy change induced by the bosons. The occupation probabilities of the bosons are described by damped Bose statistics, where the damping sets in at considerably higher energies than the neutron separation energy. At excitation energies close to or below the neutron separation energy the damping has negligible effect which implies that the phonons are allowed to be repeated several times.

The vibrational enhancement at the neutron separation energy is quite small in the QTDA method as compared to the attenuated phonon method, see Fig. 17. The QTDA gives an enhancement of the order of a few percent compared to up to a factor 7 in the attenuated phonon method. The largest vibrational enhancements

are obtained for the  $A=75$  region and for Cd isotopes in the  $A=115$  region, which is consistent with the strong (quadrupole) vibrational character of nuclei in these regions.

The QTDA phonons are microscopically built from quasi-particle excitations  $E_{\mu}^{\text{qp},i}$  with energies not much different than the QTDA phonon energies  $(\hbar\omega)_j^i$ . The way to fully account for double-counting of phonon states (Eq. 19), thus implies a small vibrational enhancement since the existence of a few low-lying collective phonons will not impact the level density if all other phonons are very non-collective. The non-collective character of most of the phonons also implies that they cannot be repeated. Phonons in the attenuated phonon model are not described microscopically, and double-counting of states may clearly appear. In addition, it assumes that each phonon can be repeated several times.

## VI. SUMMARY

A combinatorial model for the nuclear level density is presented. The model is based on the folded-Yukawa single-particle model with ground-state deformations and parameters from Ref. [21]. The model is used to calculate the neutron resonance level spacings, yielding an rms deviation of  $f_{\text{rms}} = 4.2$ . It also compares favorably with experimental level density data versus excitation energy for several nuclei in the rare-earth region as measured by the Oslo method, as well as with the cumulative level density extracted from low-energy spectra.

The role of collective enhancements has been investigated in detail. Pairing is incorporated for each individual many-body configuration, and the distribution of the pairing gaps is investigated. No sharp pairing phase transition is observed. Instead, even at the highest excitation energy considered, a non-negligible fraction of the states have a considerable pairing gap.

Rotational states are included combinatorially by a simple rotor model with a moment of inertia dependent on the deformation and pairing gap. Vibrational states are included using a Quasi-particle-Tamm-Dancoff Approximation. It is found that the vibrational enhancement in the QTDA model is very small, on the order of a few percent at the neutron separation energy.

The parity distribution in the CFY model shows large oscillatory patterns for nuclei which have large gaps in the single-particle spectrum, separating shells with different parities. This is often the case for nuclei with small deformations. The patterns are quite different from the smooth pattern of the statistical parity distribution model of Ref. [16]. The CFY model is compared to other models and to experimental data when available.

The angular-momentum distribution in the CFY model is compared to the spin cutoff model in Sec. III C. It is found that the Gaussian envelope of the spin cutoff model is in good agreement with the CFY model for high excitation energies.

## Acknowledgments

We acknowledge discussions with R. Capote, M. Guttormsen, K.-L. Kratz, T. Rauscher, A. Richter and F.-K. Thielemann. S. Hilaire and S. Goriely are acknowledged for providing data underlying Fig.14.

H. U. is grateful for the hospitality of the Los Alamos National Laboratory during several visits. S. Å. and H. U. thank the Swedish national research council (VR) for support. This work was supported by travel grants for P. M. to JUSTIPEN (Japan-U. S. Theory Institute for Physics with Exotic Nuclei) under grant number DE-FG02-06ER41407 (U. Tennessee). This work was partially carried out under the auspices of the National Nuclear Security Administration of the U. S. Department of Energy at Los Alamos National Laboratory under Contract No. DE-AC52-06NA25396 and DE-FC02-07ER41457.

- 
- [1] W. Hauser and H. Feshbach, *Phys. Rev.* **87** (1952) 366.  
 [2] T. Rauscher and F.-K. Thielemann, *Atomic Data and Nuclear Data Tables*, **75** (2000) 1.  
 [3] P. Möller, *et. al.*, *Phys. Rev. C* **79** (2009) 064304  
 [4] T. Rauscher, F.-K. Thielemann and K.-L. Kratz, *Phys. Rev. C* **56** (1997) 1613.  
 [5] H.A. Bethe, *Rev. Mod. Phys.* **9** (1937) 69.  
 [6] T. Ericson, *Adv. Phys.* **9** (1960) 425.  
 [7] S. Bjørnholm, A. Bohr and B. Mottelson, *Physics and Chemistry of Fission*, Proceedings of a Conference at Rochester (IAEA, Vienna), (1974) Vol. 1, p. 367.  
 [8] A. Bohr and B. R. Mottelson, *Nuclear Structure, Volume II* (Benjamin, Reading, MA, 1975).  
 [9] V. G. Soloviev, *Nucl. Phys.* **69** (1965) 1.  
 [10] A. Gilbert and A.G.W. Cameron, *Can. J. Phys.* **43** (1965) 1446.  
 [11] A. Bohr and B. R. Mottelson, *Nuclear Structure, Volume I* (Benjamin, Reading, MA, 1969).  
 [12] A.V. Ignatyuk, J.L. Weil, S. Raman and S. Kahane, *Phys. Rev. C* **47** (1993) 1504.  
 [13] P. Leboeuf and J. Roccia, *Phys. Rev. Lett.* **97** (2006) 010401.  
 [14] S. Hilaire and S. Goriely, *Nucl. Phys. A* **779** (2006) 63.  
 [15] S. Hilaire, J. P. Delaroche and M. Girod, *Eur. Phys. J. A* **12** (2001) 169.  
 [16] Y. Alhassid, G. F. Bertsch, S. Liu and H. Nakada, *Phys. Rev. Lett.* **84** (2000) 4313.  
 [17] Y. Alhassid, S. Liu and H. Nakada, *Phys. Rev. Lett.* **99** (2007) 162504.  
 [18] M. Horoi, J. Kaiser and V. Zelevinsky, *Phys. Rev C* **67** (2003) 054309.  
 [19] A.Schiller *et. al.*, *Nucl. Instr. Meth. Phys. Res. A* **447** (2000) 498.  
 [20] Y. Kalmykov *et.al.*, *Phys. Rev. Lett.* **99** (2007) 202502.

- [21] P. Möller, J. R. Nix, W. D. Myers and W. J. Swiatecki, Atomic Data and Nuclear Data Tables, **59** (1995) 185.
- [22] L. Bonneau, P. Quentin and P. Möller, Phys. Rev. **C 76** (2007) 024320.
- [23] P. Möller, J. R. Nix and K.-L. Kratz, Atomic Data and Nuclear Data Tables, **66** (1997) 131.
- [24] T. Døssing *et al.*, Phys. Rev. Lett. **75** (1995) 1276.
- [25] P. Möller and J.R. Nix, Nucl. Phys. **A 536** (1992) 20.
- [26] H. Olofsson, R. Bengtsson and P. Möller, Nucl. Phys. **A 784** (2007) 104.
- [27] S.G. Nilsson, Kgl. Danske Videnskab. Selskab. Mat.-Fys. Medd. **29**: No. 16 (1955).
- [28] R. Bengtsson and S. Åberg, Phys. Lett. **B 172** (1986) 277.
- [29] G. Hansen and A. S. Jensen, Nucl. Phys. **A 406** (1983) 236.
- [30] M. Guttormsen, private comm. (2009).
- [31] D. M. Brink, PhD-thesis (Oxford University, 1955).
- [32] P. Axel, Phys. Rev. **126** (1962) 671.
- [33] V. O. Nesterenko, W. Kleinig, V. V. Gudkov and J. Kvasil, Phys. Rev. **C 53** (1996) 1632.
- [34] H. Sakamoto and T. Kishimoto, Nucl. Phys. **A 501** (1989) 205.
- [35] S. Åberg, Phys. Lett. **B 157** (1985) 9.
- [36] D. J. Rowe, *Nuclear Collective Motion - Models and Theory* (Butler & Tanner Ltd, Frome and London, 1970).
- [37] A. V. Ignatyuk, *Statistical Properties of excited atomic nuclei* (Transl. from Russian) IAEA, INDC(CCP)-233(L), Vienna, IAEA 1985.
- [38] S. Goriely, S. Hilaire and A. J. Koning, Phys. Rev. **C 78** (2008) 064307.
- [39] B. Lauritzen, T. Døssing and R. A. Broglia, Nucl. Phys. **A 457** (1986) 61.
- [40] S. Åberg, Phys. Rev. Lett. **64** (1990) 3119.
- [41] V. Zelevinsky, Ann. Rev. Nucl. Part. Sc. **46** (1996) 237.
- [42] S. M. Grimes, Phys. Rev. **C 38** (1988) 2362.
- [43] N. Cerf, Nucl. Phys. **A 554** (1993) 85.
- [44] H. P. Loens *et al.*, Phys. Lett. **B 666** (2008) 395.
- [45] D. Mocolj *et al.*, Phys. Rev. **C 75** (2007) 045805.
- [46] RIPL2, Reference Input Parameter Library, IAEA-Tecdoc, 2005, available at <http://www-nds.iaea.or.at/ripl2..>
- [47] A. J. Koning, S. Hilaire and S. Goriely, Nucl. Phys. **A 810** (2008) 13.
- [48] A. C. Larsen *et al.*, Phys. Rev. **C 73** (2006) 064301.
- [49] R. Chankova *et al.*, Phys. Rev. **C 73** (2006) 034311.
- [50] S. Siem *et al.*, Phys. Rev. **C 65** (2002) 044318.
- [51] M. Guttormsen *et al.*, Phys. Rev. **C 68** (2003) 064306.
- [52] E. Melby *et al.*, Phys. Rev. **C 63** (2001) 044309.
- [53] A. Schiller *et al.*, Phys. Rev. **C 63** (2001) 021306(R).